Journal of Applied Geophysics 107 (2014) 137–148

Contents lists available at ScienceDirect

Journal of Applied Geophysics

journal homepage: www.elsevier.com/locate/jappgeo

Resolution limits for wave equation imaging

Yunsong Huang *, Gerard T. Schuster

Earth Science and Engineering, KAUST, Thuwal, Saudi Arabia

ARTICLE INFO

Article history:
Received 3 March 2014
Accepted 26 May 2014
Available online 4 June 2014

Keywords:
Wave scattering
Wave diffraction
Computational seismology
Tomography
Migration

ABSTRACT

Formulas are derived for the resolution limits of migration-data kernels associated with diving waves, primary reflections, diffractions, and multiple reflections. They are applicable to images formed by reverse time migration (RTM), least squares migration (LSM), and full waveform inversion (FWI), and suggest a multiscale approach to iterative FWI based on multiscale physics. That is, at the early stages of the inversion, events that only generate low-wavenumber resolution should be emphasized relative to the high-wavenumber resolution events. As the iterations proceed, the higher-resolution events should be emphasized. The formulas also suggest that inverting multiples can provide some low- and intermediate-wavenumber components of the velocity model not available in the primaries. Finally, diffractions can provide twice or better the resolution than specular reflections for comparable depths of the reflector and diffractor. The width of the diffraction–transmission wavepath is approximately λ at the diffractor location for the diffraction–transmission wavepath.

1. Introduction

FWI (Lailly, 1984; Tarantola, 1984, 2005), RTM (Baysal et al., 1983; McMechan, 1983; Whitmore, 1983), LSM (Dai et al., 2012; Duquet et al., 2000; Nemeth et al., 1999; Tang, 2009) and wave-equation traveltime inversion (De Hoop and van Der Hilst, 2005; Luo, 1991; Luo and Schuster, 1991; Woodward, 1989, 1992) are important tools for imaging seismic data at the engineering (Buddensiek et al., 2008), exploration (Krebs et al., 2009; Mora, 1988, 1989; Pica et al., 1990; Pratt and Goulty, 1991; Shin and Cha, 2008; Virieux and Operto, 2009; Zhou et al., 1995) and earthquake (De Hoop and van Der Hilst, 2005; Fichtner, 2011; Fichtner and Trampert, 2011a,b; Fichtner et al., 2009; Marquering et al., 1999; Tape et al., 2009; Tong et al., 1998; Van Der Hilst and Maarten, 2005) scales. In all of the above methods, the wave equation is inverted to estimate the model that minimizes, in some sense, the difference between the predicted and observed data. The main value of these wave equation-based imaging methods is that they overcome the high-frequency assumption of ray-based methods and use many, if not all, of the arrivals to reconstruct a finely detailed earth model. The hope is to find models with spatial resolution of one-half wavelength, and perhaps even better if evanescent energy can be exploited (de Fornel, 2001; Fink, 2008; Schuster et al., 2012). The main limitations of wave equation imaging are computational cost and extensive preprocessing of the data, compared to the ray-based methods.

To optimize the use of wave equation imaging one must understand its limits of spatial resolution. Without this understanding, models can be over parameterized and lead to solutions that honor the data but violate the wavelength-based resolution limits of wave propagation. Such models should be avoided in our attempts to understand the earth.

In the last 30 years, there has been much progress in mathematically defining the resolution limits of seismic images. The two most important categories of seismic imaging and their resolution limits are for traveltime tomography and reflection imaging.

1.1. Resolution limits for traveltime tomography

In raypath traveltime tomography, the velocity is updated only along the raypath that connects the source at s with the receiver at g, whereas in finite-frequency travel time tomography, velocity updates can be confined to the first Fresnel zone for the specified source–receiver pair (Harlan, 1990). He states, "band-limited waves can follow paths that are not Fermat raypaths and still cover the distance between two points in almost the same time. All arriving waves that are delayed by less than half a wavelength will add constructively to the first arrival."

As an example, the raypaths and Fresnel zones for reflection and transmission arrivals are illustrated in Fig 1. A point x is in the FZ if and only if it satisfies the following condition (Cerveny and Soares, 1992; Kravtsov and Orlov, 1990):

$$|\tau_{sx} + \tau_{xg} - \tau_{sg}| \le T/2, \tag{1}$$

Abbreviations: LSM, least squares migration; FWI, full waveform inversion; FZ, Fresnel zone; MVA, migration velocity analysis; RTM, reverse time migration.

* Corresponding author at: Room 3124, Building 1, KAUST, Thuwal, Saudi Arabia 23955-6900. Tel.: +966 128080296.
E-mail addresses: yunsong.huang@kaust.edu.sa (Y. Huang), gerard.schuster@kaust.edu.sa (G.T. Schuster).

http://dx.doi.org/10.1016/j.jappgeo.2014.05.018
0926-9851/

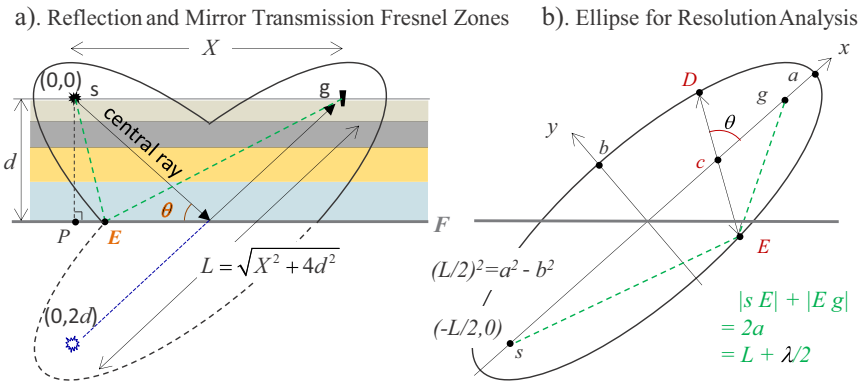

Fig. 1. a) First Fresnel zones for the specular reflection and for the transmission arrival excited by the mirror source at (0,2*d*). In the latter case, the velocity model below the reflector (the thick horizontal line denoted by *F*) has been extended to be the mirror-reflection of the velocity model above the reflector. Colored layers denote the possibility that the velocity model is multilayered, instead of homogeneous. In this case, although the Fresnel zone is not an ellipse, the horizontal resolution can be computed approximately involving the RMS velocity v_{RMS} (see Appendix A). b) An ellipse intersected by a line segment *DE*, where its length $\overline{DE} = \frac{2ab\sqrt{b^2\cos^2\theta + (a^2-c^2)\sin^2\theta}}{b^2\cos^2\theta + a^2\sin^2\theta}$ defines the resolution limit (see Appendix A).

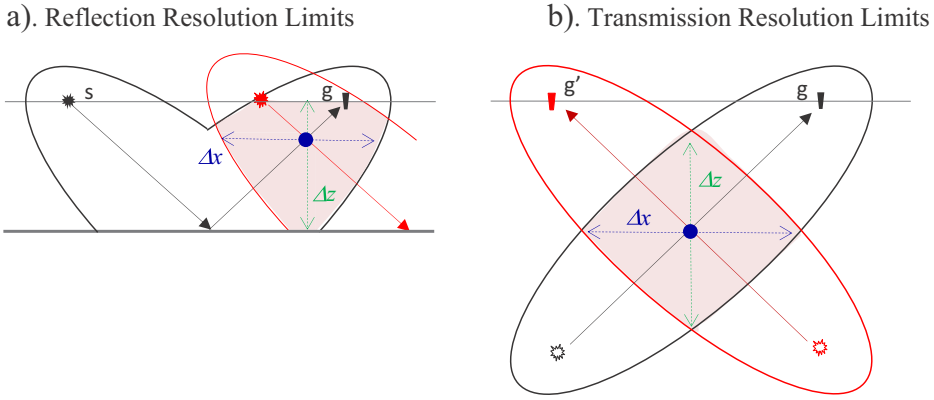

Fig. 2. Same as Fig. 1 except there is an additional source–receiver pair. The minimum width and height of the shaded intersection zone define, respectively, the effective horizontal Δx and vertical Δz resolution limits of the traveltime tomogram at ●.

where, T is the dominant period of the source wavelet, τ_{sx} is the traveltime for a particular type of wave to propagate from s to the trial image point at x, and τ_{sg} is the traveltime to propagate from s to the specified geophone at g.

In a homogeneous medium, the maximum width of the first Fresnel zone can be shown (Williamson, 1991) to be proportional to $\sqrt{\lambda L}$, where L is the source–receiver distance and λ is the dominant wavelength. Thus, widening the distance between the source and receiver lowers the spatial resolution of the traveltime tomogram. More generally, Appendix A derives the formula for the length between any two points on opposite sides of the ellipse, which provides the horizontal resolution limit for any orientation of the ellipse. In addition, Appendix A derives the formula for horizontal resolution in multilayered, rather than homogeneous, media.

The effective spatial resolution limits Δx and Δz of traveltime tomograms can be estimated (Schuster, 1996) as the minimum width and height of the *intersection* of first Fresnel zones at the trial image point. This can be seen by assuming the L_2 traveltime misfit $J = \sum_i J_i$, where J_i denotes the traveltime misfit owing to the i^{th} source–receiver pair, and assuming model consistency, i.e., there exists a velocity model that can explain all observed traveltime. If a part of the trial model lies furthest from the Fresnel zone prescribed by the i^{th} source–receiver pair, then J_i will dominate and steepest descent updates will propel this trial model point towards the center of this Fresnel zone. The rule that the traveltime error is less than $T/2$ for all source–receiver pairs defines an intersection of all the individual Fresnel zones. As an example, Fig. 2 illustrates the intersection zone for both a) reflection and b) transmission rays. At any point on the central raypath, the narrowest width is along the line perpendicular to this ray, which also defines the direction of best resolution. Thus, *a horizontal ray gives the best vertical resolution while a vertically oriented ray provides the best horizontal resolution for transmission tomography*, where the velocity is updated by smearing residuals along the first FZ (also referred to as a wavepath). As will be shown in the next section, this rule of thumb is also true for transmission wavepaths in FWI tomograms, except the *waveform residual* is smeared along the associated wavepath.

1.2. Resolution limits for reflection imaging

A seismic migration image is formed by taking the reflection energy arriving at time $\tau_{sx} + \tau_{xg}$ and smearing (Claerbout, 1992) it along the appropriate ellipse in the model-space coordinates x (see Fig. 3a). For several traces, the migration image in Fig. 3b is formed by smearing[1] and summing the reflection energy along the appropriate ellipses in the model space. It is obvious that the *narrowest horizontal slice of the fat ellipse is for a trial image point at the far left and far right of the ellipse*

[1] The seismic amplitude is smeared over the thick ellipse shown in Fig. 3a, where the period T of the trace's source wavelet determines the thickness of the fat ellipse in (x, z) space; Fig. 3b illustrates that the minimum thickness of the fat ellipse as 0.5λ.

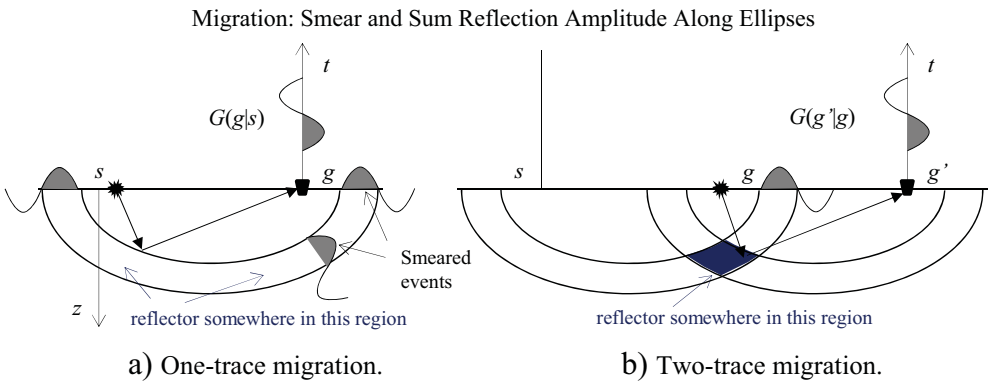

Fig. 3. Migration is the smearing and summation of trace amplitudes along the appropriate fat ellipses in (x, z) for each source–receiver pair $\mathbf{s} - \mathbf{g}$ (Claerbout, 1992). Migration of two traces in b) has better spatial resolution than migrating just one trace in a), and the minimum thickness of each fat ellipse is 0.5λ, where T is the dominant period of the source wavelet.

to give the best horizontal resolution in the reflection migration image. We also see that the narrowest vertical slice is directly beneath the midpoint of the source–receiver pair to give the best vertical resolution. For post-stack data, these resolution limits are given on the right side of Fig. 4e, which say that the far-offset (near-offset) trace from a trial image point gives the best horizontal (vertical) resolution.

The resolution limits for migration (Berkhout, 1984; Chen and Schuster, 1999; Safar, 1985; Vermeer, 1997) are equivalent to those for linearized inversion in a homogeneous (Devaney, 1984; Wu and Toksoz, 1987) and an inhomogeneous medium (Beylkin, 1985) with smooth velocity variations. The key idea is that the model wavenumber vector $\mathbf{k}$ can be equated to the sum of the source–scatterer and geophone–scatterer wavenumbers $\mathbf{k} = \mathbf{k}_{sr_o} + \mathbf{k}_{gr_o}$ shown in Fig. 5. If $\mathcal{D}$ defines the range of wavenumbers available from the source–receiver positions, then the horizontal Δx and vertical Δz spatial resolution limits of the migration image are defined as

$$\Delta x = \min_{\mathcal{D}}\left[\frac{2\pi}{k_x}\right] = \min_{\mathcal{D}}\left[\frac{2\pi}{k_{sx_o} + k_{gx_o}}\right], \Delta z = \min_{\mathcal{D}}\left[\frac{2\pi}{k_z}\right] = \min_{\mathcal{D}}\left[\frac{2\pi}{k_{sz_o} + k_{gz_o}}\right]. \quad (2)$$

In the far-field approximation, these limits are given in Fig. 4e for post-stack migration.

The above resolution analysis has been developed for migration and traveltime tomography. Until now, there has not been a comprehensive treatment of the resolution limits associated with LSM. We now present

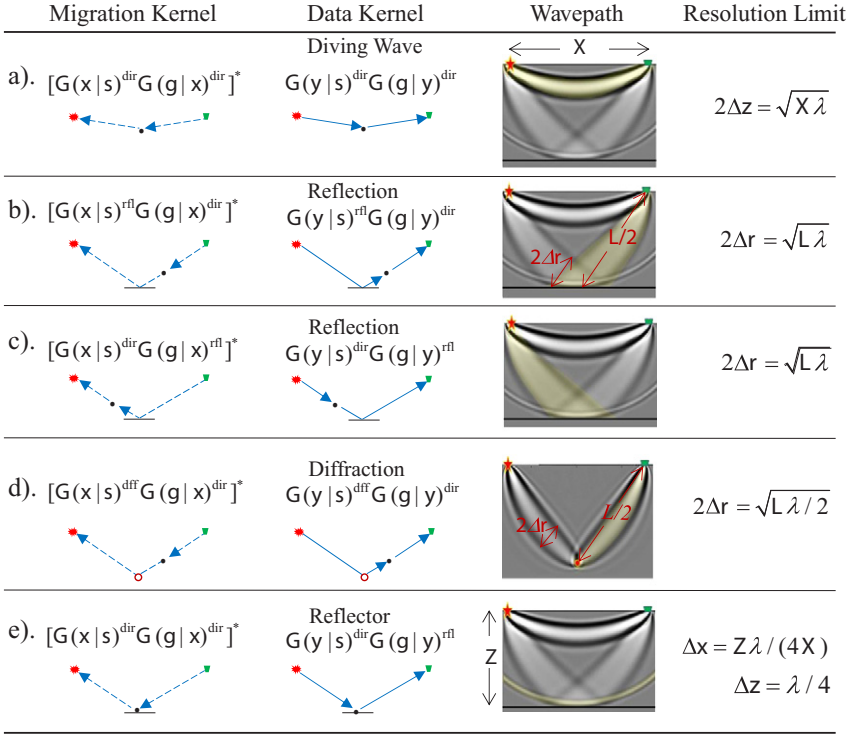

Fig. 4. Migration-data kernels, associated wavepaths, and approximate resolution limits along the middle of the wavepaths for (a–d). Here, the dashed lines in the first column represent the raypaths associated with the conjugated kernels; the solid lines with arrows in the second column represent the raypaths associated with the data kernels; the trial image points x and y are represented by •; the diffractor in (d) is denoted by ; and the resolution limit perpendicular to the wavepath is denoted by $2\Delta r$. The resolution limits for reflection migration in (e) are for post-stack data, where X corresponds to aperture width, and Δx and Δz correspond to the skinniest width and thickness of the fat migration ellipse.

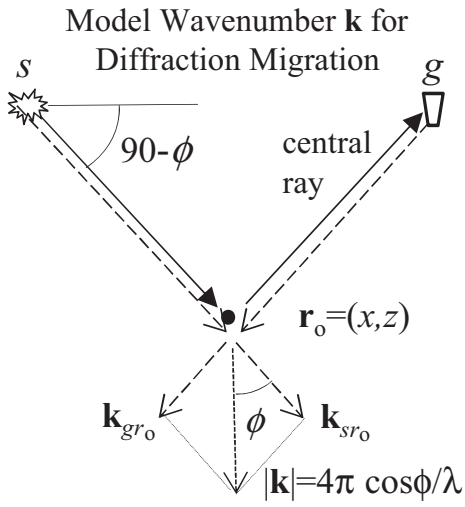

Fig. 5. Scatterer at $\mathbf{r}_o = (x, z)$ where the sum of the dashed source–scatterer $\mathbf{k}_{sr_o}$ and geophone–scatterer wavenumbers $\mathbf{k}_{gr_o}$ is equal to the recoverable model wavenumber $\mathbf{k}$. Solid rays define the central raypath.

such an analysis by applying an asymptotic analysis to the model resolution function for LSM. The resulting resolution formulas can be used to better understand and optimize the resolution characteristics of FWI, LSM, and RTM.

This paper is divided into three parts. The introduction heuristically explains how wavepaths are used to estimate resolution for both traveltime tomography and migration. This leads to an intuitive description of spatial resolution as the minimum width and height of the intersection of Fresnel zones at the trial image point. The next part validates this heuristic definition by rigorously deriving the resolution limits for each type of wavepath, and explains their relationship to the acquisition geometry. Finally, a discussion and summary are given.

2. Born forward and adjoint modeling

The model resolution function $\mathbf{L}^\dagger\mathbf{L}$ is a product of forward $\mathbf{L}$ and adjoint $\mathbf{L}^\dagger$ modeling operators under the Born approximation (Stolt and Benson, 1986). We now define the equations for these modeling operators.

2.1. Born forward modeling

The trace $d(\mathbf{g}|\mathbf{s})$ excited by a harmonic point source at $\mathbf{s}$ and recorded by a geophone at $\mathbf{g}$ is given by the Born modeling equation:

$$\delta d(\mathbf{g}|\mathbf{s}) = \omega^2 \int_\Omega G(\mathbf{g}|\mathbf{x})\delta m(\mathbf{x})G(\mathbf{x}|\mathbf{s})dx^2 \rightarrow \delta\mathbf{d} = \mathbf{L}\delta\mathbf{m}, \tag{3}$$

where $G(\mathbf{g}|\mathbf{x})$ is the Helmholtz Green's function for the background velocity model, the model function perturbed from the background model is given by $\delta m(\mathbf{x}) = 2\delta s(\mathbf{x})s(\mathbf{x}) \rightarrow \delta\mathbf{m}$, $s(\mathbf{x})$ is the background slowness model, $\delta s(\mathbf{x})$ is the perturbation of the slowness field, and ω is the angular frequency. For notational economy, this equation can be represented in operator notation by $\delta\mathbf{d} = \mathbf{L}\delta\mathbf{m}$, where $\delta\mathbf{d}$ represents the scattered seismic field $\delta d(\mathbf{g}|\mathbf{s})$ under the weak scattering approximation, $\mathbf{L}$ represents the integral operator, and Ω defines the integration points in the model region.

The integration in Eq. (3) is over the entire model space, but if the trace is windowed about a specific event then the integration can be approximated by that over the event's first Fresnel zone associated with the specific source–receiver pair. For example, if the trace only contains the transmitted arrival, then $\Omega = \Omega_{trans.}$ defines the points in the yellow colored wavepath in Fig. 4a of the diving wave's first Fresnel zone; only velocity perturbations in this zone will significantly affect the character of the diving wave arrival in the trace.

2.2. Born adjoint modeling

Eq. (3) can be inverted by the iterative steepest descent formula

$$\delta m(\mathbf{x})^{k+1} = \delta m(\mathbf{x})^k - \alpha\, \delta m(\mathbf{x})^{mig}, \tag{4}$$

where the misfit gradient $\delta m(\mathbf{x})^{mig}$ is given by the Born adjoint modeling equation

$$\delta m(\mathbf{x})^{mig} = \omega^2 \int_D G(\mathbf{g}|\mathbf{x})^* G(\mathbf{x}|\mathbf{s})^* \delta d(\mathbf{g}|\mathbf{s}) dx_g dx_s \rightarrow \delta\mathbf{m}^{mig} = \mathbf{L}^\dagger\delta\mathbf{d}, \tag{5}$$

and the integration of points in D is over the range of the horizontal source and receiver coordinates along the horizontal recording line at $z = 0$. Here, $\delta d(\mathbf{g}|\mathbf{s}) = d(\mathbf{g}|\mathbf{s}) - d(\mathbf{g}|\mathbf{s})^{obs}$, $\mathbf{L}^\dagger$ represents the adjoint of the modeling operator $\mathbf{L}$, the step length is denoted by α, $d(\mathbf{g}|\mathbf{s})$ is the trace predicted from the estimated slowness model, and the observed trace is represented by $d(\mathbf{g}|\mathbf{s})^{obs}$. The misfit gradient symbol $\delta m(\mathbf{x})^{mig}$ is superscripted by *mig* because it also represents the migration of the residual. In fact, the first iteration $k = 0$ of Eq. (5) represents the reverse time migration of the scattered data recorded at the surface.

If the windowed event is the reflection, Eq. (5) says that the velocity model is updated by smearing the residual[2] along the yellow colored rabbit ears[3] in Fig. 4b–c and the yellow ellipse in Fig. 4e. Smearing residuals along the rabbit ears (ellipse) with the b–c (e) migration kernel updates the low-wavenumber (high-wavenumber) portion of the velocity model (Liu et al., 2011; Mora, 1989; Zhou et al., 1995). The spatial resolution limits Δx and Δz associated with any point along the central rays are determined by the, respectively, horizontal and vertical widths of the first Fresnel zone.

3. Model resolution function and FWI resolution limits

In the Introduction, the model resolution limits were defined for traveltime transmission tomography and reflection migration, where λ is considered as the dominant wavelength. For a band-limited source wavelet, the dominant wavelength is typically associated with the peak frequency. Now the model resolution limits will be derived for FWI by applying asymptotic analysis to the model resolution function that relates the model $\delta\mathbf{m}$ to the reconstructed image $\delta\mathbf{m}^{mig}$. Note in passing that in practice, FWI is typically carried out in multiscale (Bunks et al., 1995; Sirgue and Pratt, 2004) such that at a given stage, FWI only concerns the source wavelet filtered into a narrowband. In this case, the pertinent λ still belongs to the peak frequency of the narrowband source. In contrast, LSM is carried out with the original band-limited source wavelet. Because the inversion process of LSM tends to deconvolve the source wavelet, the resolution limits are defined asymptotically by the λ associated with the upper cutoff frequency of the source wavelet.

[2] The residual can be either the traveltime residual or the waveform residual.

[3] There are two steps for creating an upgoing reflection wavepath: first, generate the migration image and use the reflectors as exploding sources that explode at the traveltime from the source to the reflector. Then, fire off these exploding reflectors to get the upgoing reflection fields $U(\mathbf{x}, t)$. The upgoing rabbit ear wavepath is computed by taking the zero-lag correlation between $U(\mathbf{x}, t)$ and the backpropagated data $B(\mathbf{x}, t)$.

3.1. Model resolution equation: $\mathbf{m}^{mig} = \mathbf{L}^{\dagger}\mathbf{L}\mathbf{m}$

The forward and adjoint modeling equations can be combined to give the equation for model resolution, i.e., plugging Eq. (3) into Eq. (5) gives

$$\delta m(\mathbf{x})^{mig} = \omega^4 \int_D \overbrace{[G(\mathbf{g}|\mathbf{x})G(\mathbf{x}|\mathbf{s})]^*}^{\text{migration kernel}} \int_\Omega \overbrace{G(\mathbf{g}|\mathbf{y})G(\mathbf{y}|\mathbf{s})}^{\text{data kernel}} \delta m(\mathbf{y}) dy^2 dx_g dx_s, \quad (6)$$

or in more compact notation

$$\delta \mathbf{m}^{mig} = \mathbf{L}^{\dagger}\mathbf{L}\delta\mathbf{m}. \quad (7)$$

The kernel for the operator $\mathbf{L}^{\dagger}\mathbf{L}$ is related to the model resolution matrix (Menke, 1989) and is interpreted as the point spread function (Schuster and Hu, 2000) similar to that used in optics, except here, if $\delta m(\mathbf{y}) = \delta(\mathbf{y} - \mathbf{r}_o)$, it is the migration response to a point slowness perturbation in the model at $\mathbf{r}_o$. The ideal response to a point slowness anomaly is the same point with perfect resolution.

For a two-layer medium, the above Green's function can be decomposed into its direct and reflection components:

$$\begin{aligned} G(\mathbf{g}|\mathbf{x}) &= G(\mathbf{g}|\mathbf{x})^{dir} + G(\mathbf{g}|\mathbf{x})^{rfl}, \\ G(\mathbf{s}|\mathbf{x}) &= G(\mathbf{s}|\mathbf{x})^{dir} + G(\mathbf{s}|\mathbf{x})^{rfl}, \end{aligned} \quad (8)$$

where $G(\mathbf{g}|\mathbf{x})^{dir}$ and $G(\mathbf{g}|\mathbf{x})^{rfl}$ are, respectively, the Green's function for the direct wave and upgoing reflection in the upper layer. Inserting Eq. (8) into the migration kernel in Eq. (6) results in the five migration kernels shown in Fig. 4, each of which is used to smear residuals along one of the five yellow colored wavepaths (Liu et al., 2011; Zhan et al., 2014).

3.1.1. Reflection migration

Reflection migration smears residuals along the yellow colored ellipse in Fig. 4e for a specified source and receiver pair. When two traces are migrated, Fig. 3b suggests that the minimum width and height of the intersecting fat ellipses define the resolution limits of reflection migration.

The formulas for migration resolution limits were more rigorously derived (Beylkin, 1985) by applying the migration kernel to traces that only contain the diffraction arrival from a single diffractor. For a localized scatterer[4] in a background medium with smooth velocity variations, Eq. (6) asymptotically becomes the Fourier integral over the model wavenumbers k_x and k_z:

$$\delta m(\mathbf{x})^{mig} = \alpha \int_{\mathcal{D}} e^{-i\mathbf{k}\cdot\mathbf{x}} \delta M(\mathbf{k}) J^{-1} dk_x dk_z, \quad (9)$$

where α is related to geometrical spreading, J is the Jacobian, which is derived in Appendix C, and the range of model wavenumbers $\mathcal{D}$ in the integral depends on the range of source–receiver pairs. In fact, the model wavenumber vector $\mathbf{k}$ can be equated to the sum of the source–scatterer and geophone–scatterer wavenumbers $\mathbf{k} = \mathbf{k}_{gr_o} + \mathbf{k}_{sr_o}$ shown in Fig. 5. We will now show how Eqs. (6) and (9) can be used to estimate the resolution limits of the other wavepaths in Fig. 4a–d.

3.1.2. Diving wave transmission

Migration of the diving wave residual along the yellow transmission wavepath in Fig. 4a provides the low-wavenumber velocity update for waveform inversion (Mora, 1989; Zhou et al., 1995), or wave equation traveltime inversion (Luo and Schuster, 1991; Woodward, 1989, 1992) if the trace residual is replaced by the recorded trace weighted by the traveltime residual. The boundary of the first Fresnel zone wavepath[5] is defined by values of $\mathbf{x}$ for the delayed diving wave time $\tau_{sg}^{dive} + T/2 = \tau_{sx} + \tau_{xg}$, where τ_{sg}^{dive} is the diving wave traveltime at the geophone location $\mathbf{g}$. As illustrated in Fig. 2b, the minimum width and height of the intersecting fat ellipses define the effective resolution limits of transmission tomography (Williamson, 1991) or transmission migration (Sheley and Schuster, 2003).

More rigorously, Appendix B shows that the model resolution Eq. (6) for diving waves can be transformed into the Fourier integral

$$\delta m(\mathbf{x})^{mig} = \alpha \int_{\mathcal{D}_{r_o}} e^{-i\mathbf{k}\cdot\mathbf{x}} \delta M(\mathbf{k}) J^{-1} dk_x dk_z, \quad (10)$$

where α is a term related to geometrical spreading and $\mathcal{D}_{r_o}$ defines the range of source–geophone pairs whose first Fresnel zone wavepaths visit the scatterer localized at $\mathbf{r}_o$. The formulas for resolution limits are the same as in Eq. (2), except $\mathcal{D}$ is replaced by $\mathcal{D}_{r_o}$.

The range of allowable source–geophone pairs (see Sheng and Schuster, 2003) in $\mathcal{D}_{r_o}$ is illustrated in Fig. 6b, where only the sources between the blue and red stars will contribute to the slowness update around the scatterer point at $\mathbf{r}_o$. This differs from the Fourier integral in Eq. (9) for diffraction imaging where *all* source–geophone pairs contribute to the integration domain in $\mathcal{D}$ for a recorded diffraction. Hence, the resolution limits for migrating transmission residuals with the kernel $[G(\mathbf{g}|\mathbf{x})^{dir}G(\mathbf{x}|\mathbf{s})^{dir}]^*$ should be worse than migrating diffraction residuals with the same kernel.

The precise connection between intersecting wavepaths in Fig. 2b, the range of available wavenumbers, and resolution limits in Eq. (2) can be made by assuming a homogeneous medium. In this case, Fig. 7 shows that the half-width Δz of the first Fresnel zone at the point midway between the source and geophone is equal to

$$\Delta z = \sqrt{L\lambda/4}, \quad (11)$$

where L is the distance between the source and geophone, which is equal to that given by Eq. (2). It also shows that Δz is inversely proportional to the sum of the source–scatterer and geophone–scatterer wavenumbers, implying that $\min 1/k_z$ is equivalent to finding the width of the wavepath intersections in Fig. 2b.

For a single source–geophone pair, the *best direction of transmission spatial resolution for a slowness anomaly midway between the source and geophone is perpendicular to the central ray*. This means that a slowness anomaly moved perpendicular to the ray from the central ray would lead to the most noticeable change in the transmission arrival. The *worst direction of spatial resolution is along the ray itself* because the slowness anomaly can be slid along it without changing the traveltime; moreover, the model wavenumber $\mathbf{k} = \mathbf{k}_{sx} + \mathbf{k}_{xg}$ is zero all along the transmission central ray.

3.1.3. Reflection–transmission

Migrating the reflection arrival with any of the kernels in the first column of Fig. 4b–c leads to the low-wavenumber velocity update along the rabbit-ear wavepaths in Fig. 4b–c or Fig. 1a.

The corresponding resolution formula for the rightmost rabbit-ear wavepath is

$$\delta m(\mathbf{x})^{mig} = \omega^4 \int_{D_{r_o}} \left[G(\mathbf{g}|\mathbf{x})^{dir} G(\mathbf{x}|\mathbf{s})^{refl}\right]^* \int_{\Omega_{gs}} G(\mathbf{g}|\mathbf{y})^{dir} G(\mathbf{s}|\mathbf{y})^{refl} \delta m(\mathbf{y}) dy^2 dx_g dx_s, \quad (12)$$

and, as before, can be analyzed for the resolution limits. However, now the asymptotic Green's functions for the transmitted arrival $G(\mathbf{g}|\mathbf{x})^{dir}$ and the reflection field

$$G(\mathbf{x}|\mathbf{s})^{refl} = A_{sx}^{refl} e^{-i\omega\tau_{sx}^{refl}}, \quad (13)$$

are plugged into Eq. (12) to give the resolution limits for updating the velocity by smearing the reflection residual along the rabbit ears. Here, A_{sx}^{refl} accounts for amplitude and phase effects from geometrical

[4] We will assume a 2D model where the "point" source and scatterer are equivalent to a line source and a line scatterer, with no field variations along the y-axis.

[5] Dahlen (2004) refers to the shape of a diving wavepath as a banana.

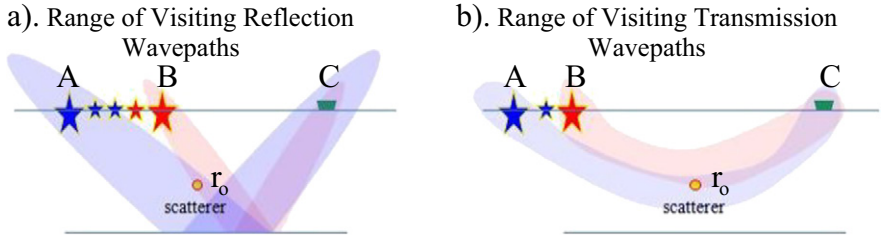

Fig. 6. Range of sources (★) that generate a) reflection and b) transmission wavepaths that visit the scatterer (∘). Here, the wavepath is approximated by the first Fresnel zone for the specified source and geophone pair.

spreading and the reflection coefficient; τ_{sx}^{refl} is the time it takes reflection energy to propagate from the source at s to the listener at $\mathbf{x} = \mathbf{r}_o$ along the specular dashed raypath in Fig. 1a.

Estimating the resolution limits for the rabbit-ear wavepaths will result in model resolution formulas similar to that given in Fig. 4a for transmission imaging. This can be understood without going through the detailed algebra by recognizing that the upgoing reflection wavepath (rightmost rabbit ear in Fig. 1a) is identical to the transmission wavepath in Fig. 1b above the interface. This is denoted as a mirror transmission wavepath because it coincides with the first Fresnel zone for a source at the mirror position $(0, 2d)$ in a homogeneous velocity. Thus, the reflection traveltime in a) is identical to the transmission traveltime in b) for any receiver at $\mathbf{r}_o$. This means that the resolution limits defined by Eq. (2) are applicable to the transmission wavepaths in Fig. 1b and the reflection wavepaths in Fig. 1a. However, the range of available wavenumbers for the traces recorded at $\mathbf{g}$ is determined by the limited range of sources in Fig. 6a that allow for the intersection of their first Fresnel zones with the scatterer. For example, the resolution limit $2\Delta r$ perpendicular to the ray at the midpoint should be equal to the $2\Delta r = \sqrt{\lambda L}$ in Fig. 1a, except the total length of the reflection ray is $L = \sqrt{X^2 + 4d^2}$.

3.1.4. Diffraction–transmission

How do the resolution characteristics of the diffraction–transmission wavepaths in Fig. 4d compare to those for the reflection–transmission wavepaths in Fig. 4b–c? Fig. 8 suggests that the diffraction resolution limit will be significantly better because the diffraction propagation distance is effectively halved, leading to a narrower wavepath. This means

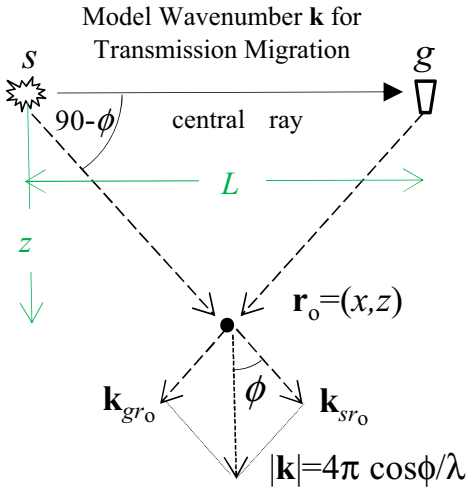

Fig. 7. Transmission ray and scatterer at $\mathbf{r}_o = (x, z)$ where $x = L/2$ for a homogeneous medium. We assume $L \gg z$ and z is equal to the half-width $z \approx \sqrt{\lambda L/4}$ of the 1st Fresnel zone in a homogeneous medium. In this case, $\cos\phi = z/\sqrt{L^2/4 + z^2} \approx 2z/L$; inserting the half-width formula gives $\cos\phi = \sqrt{\lambda/L}$ so $k_z = 4\pi \cos\phi/\lambda = 4\pi/\sqrt{L\lambda}$.

that, if the waveform residuals are used to update the velocity, then the diffraction updates will have significantly better resolution than the reflection updates.

The resolution limits for diffraction–transmission migration can be quantified according to Eq. (11), to obtain that the maximum resolution limits perpendicular to the diffraction and reflection central rays should be, respectively, $2\Delta r^{diff} \approx \sqrt{\lambda L/2}$ and $2\Delta r^{refl} \approx \sqrt{\lambda L}$. In this case, $L/2$ is the effective length of the central ray between the geophone and the scatterer in Fig. 8a. These limits can be rigorously derived by defining the diffraction Green's function $G(\mathbf{x}|\mathbf{s})^{diff}$ as

$$G(\mathbf{x}|\mathbf{s})^{diff} = A^{diff}_{sx_ox} e^{-i\omega\left(\tau_{sx_o} + \tau_{x_ox}\right)}, \tag{14}$$

where the diffractor is located at $\mathbf{x}_o$, the trial image point is at $\mathbf{x}$, and $A^{diff}_{sx_ox}$ accounts for the effects of geometrical spreading, reflection amplitude, and phase changes due to scattering. Replacing the migration kernel in Eq. (6) by $[G(\mathbf{g}|\mathbf{x})^{diff} G(\mathbf{x}|\mathbf{s})^{dir}]^*$ and the data kernel by $[G(\mathbf{g}|\mathbf{y})^{diff} G(\mathbf{y}|\mathbf{s})^{dir}]$, and using the explicit expression for the Green's functions yields the model resolution function for diffraction imaging:

$$\delta m(\mathbf{x})^{mig} = \omega^4 \int_D \left[A^{diff}_{sx_ox} A_{gx}\right]^* \int_\Omega A^{diff}_{sx_oy} A_{gy}\, e^{i\omega\left(\tau_{gx} - \tau_{gy} + \tau_{x_ox} - \tau_{x_oy}\right)} dy^2 dx_g dx_s. \tag{15}$$

The salient difference between this formula and the one for reflections in Eq. (B.4) is that τ_{x_ox} and τ_{x_oy} replace τ_{sx} and τ_{sy}. This says that the diffraction wavepath is generated by a "virtual" source at the diffractor $\mathbf{x}_o$ rather than at the actual source location $\mathbf{s}$. Hence, the diffraction wavepath should be thinner than the specular reflection wavepath in Fig. 8. In addition, every source–geophone pair has a diffraction wavepath that intersects the diffractor. This means that, similar to diffraction migration, many more diffraction wavenumbers will be available for velocity updates compared to specular reflection–transmission wavepaths.

3.2. Wavelength imaging at the diffractor

Figs. 4d and 8a illustrate that the width of the diffraction–transmission wavepath is proportional to λ at the diffractor location. This can be mathematically proven by locating the point $\mathbf{E}$ on the Fig. 1b ellipse so that the line through it and the focus at $\mathbf{g}$ is perpendicular to the elliptical axis. The distance between $\mathbf{E}$ and $\mathbf{g}$ is denoted as $\overline{Eg}$. In the far-field approximation, $L \gg \overline{Eg} = z_o$ so we can approximate the ellipse formula for the first Fresnel zone centering about $\mathbf{g}$ as

$$\lambda/2 = \sqrt{z_o^2 + L^2} + z_o - L \approx z_o. \tag{16}$$

This suggests that the resolution limit of the updated velocity model is about λ near the scatterer, which is much finer than the resolution limit of $\sqrt{L\lambda/4}$ along the middle of the Fig. 8a wavepath. This unexpectedly high-resolution limit near the reflector boundaries can be observed in wave equation reflection traveltime (Zhang et al., 2012) and tomograms of MVA.

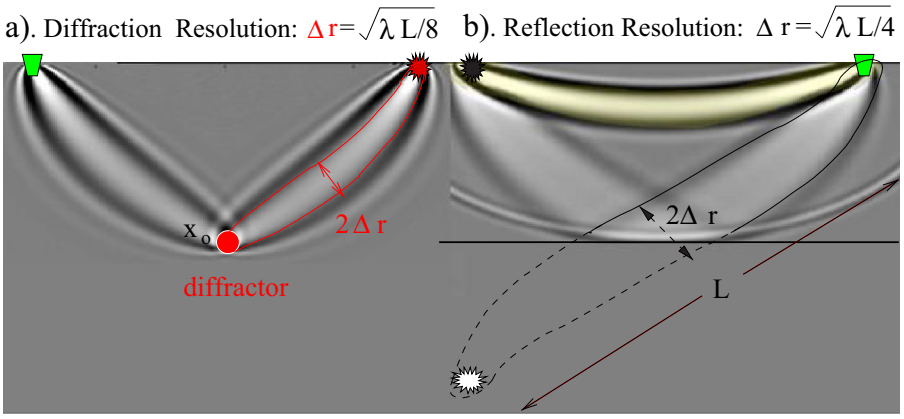

Fig. 8. Wavepaths for migrating a) diffraction (red ellipse) and b) specular reflection (black ellipse) events along their transmission wavepaths. The diffraction resolution limit $2\Delta r$ perpendicular to the widest part of the diffraction wavepath is $1/\sqrt{2}$ of that for the specular reflection. Dashed wavepath in b) is the mirror image of the source-side wavepath, with the mirror source denoted by the white star. These wavepaths were obtained by first generating acoustic data for a) a diffractor model and b) a two-layer reflector model. Windowing about the scattered arrivals, the diffraction and reflection traces were then migrated, respectively, with the kernels $[G(\mathbf{g}|\mathbf{x})^{diff}G(\mathbf{x}|\mathbf{s})^{dir}]^*$ and $[G(\mathbf{g}|\mathbf{x})^{dir}G(\mathbf{x}|\mathbf{s})^{dir}]^*$.

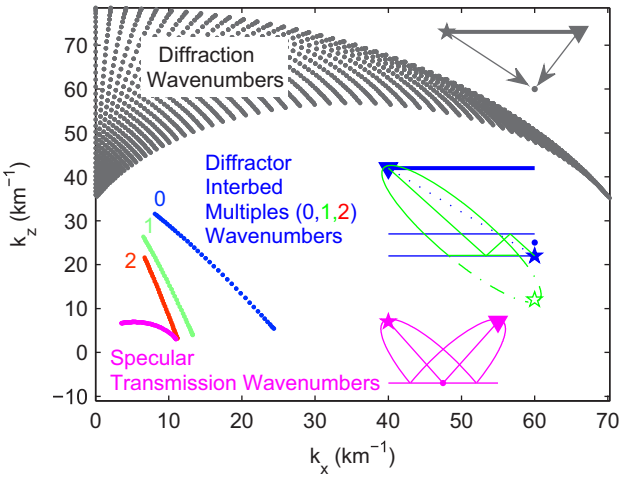

Fig. 9. Wavenumbers recovered by (i) diffraction migration (denoted by gray dots) have much higher values than those (denoted by thick magenta curve) recovered by (ii) specular transmission migration. Wavenumbers recovered by (iii) interbed multiples, of orders 0, 1, and 2, originate from a diffractor, are denoted by blue, green and red dots, respectively. These wavenumbers somewhat bridge the gap between cases (i) and (ii). The acquisition geometry is a 4 km long line of geophones and sources on the top interface, with the trial image point, denoted by •, at depth 1 km. The diffractor in case (iii) is 80 m below the trial image point.

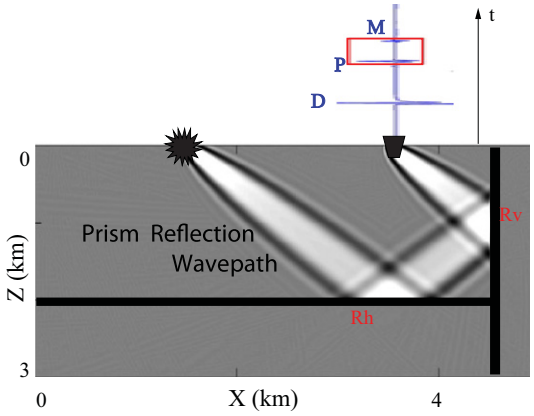

Fig. 10. Prism wavepath due to a horizontal and a vertical reflector (Rh and Rv, respectively) and a trace computed by a finite-difference solution to the wave equation. D denotes the direct arrival; P denotes the primary reflection from Rh; and M denotes the two-fold reflection from Rh and Rv. RTM was applied to the windowed events (P and M in the rectangle) to produce this wavepath.

To illustrate the range of wavenumbers estimated from diffraction and transmission migration, Fig. 9 depicts the low wavenumbers (magenta dots) of the model recovered with transmission migration (see Fig. 7) and the higher wavenumbers (gray dots) recovered by diffraction migration (Fig. 5). Note the large gap between the recovered low- and high-wavenumber spectra, which will be denoted as the missing intermediate wavenumbers. The absence of such intermediate model wavenumbers is a serious challenge for waveform inversion, which will be addressed in the next section.

4. Filling in the model spectrum with multiples

The previous sections derived the model resolution equations for diving waves, primaries, and diffractions. What are the resolution benefits for migrating multiples,[6] particularly prism waves or interbed multiples? The short answer is that their associated central rays are longer than those of primaries, so their first Fresnel zones should be wider. This means that they can reconstruct low-wavenumber and intermediate-wavenumber models that can only be inverted with primaries at impractically wide source–geophone offsets or using sources with unrealistic low frequencies.

4.1. Lower wavenumber resolution with prism waves and free-surface multiples

To demonstrate the enhanced wavenumber coverage of multiples, the point-source response of the yellow vertical reflector in Fig. 10 is computed by a finite-difference method. The trace is windowed about the reflections and then migrated by RTM to get the prism wavepath image (Dai and Schuster, 2013). As the length L of the prism ray gets longer, the wavepath becomes thicker by $\sqrt{\lambda L}$. In this way, the deep

[6] excluding certain multiples such as ghosts that may impair image resolution.

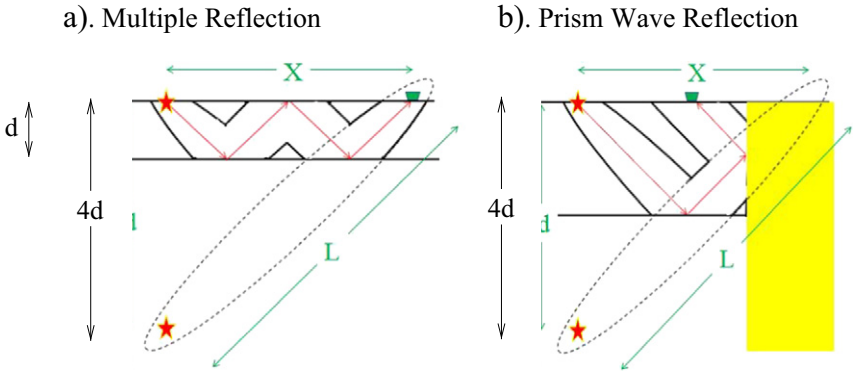

Fig. 11. Wavepaths for a) the 1st-order free-surface multiple and b) the prism-wave reflection from the yellow block. Note, the source–geophone offset for b) is about 1/2 that for a), and the dashed ellipse is the wavepath for the mirror source at the bottom left.

prism-reflection wavepath provides lower wavenumber information about the model compared to primaries. Such low wavenumbers are at the top of the FWI wish list for providing a good starting model for subsalt imaging.

Another example is shown in Fig. 11. Here, the prism-wave reflection in b) achieves the same low-wavenumber resolution as the 1st-order free-surface multiple in a), but only requires about 1/2 the source–geophone offset of a). The deeper the reflector for the free-surface multiple is, the thicker is the wavepath and the lower is the wavenumber in the estimated model.

4.2. Intermediate-wavenumber resolution with interbed multiples

Fig. 9 illustrates that transmission tomography (smearing residuals along rabbit ears) fills in the low wavenumber part of the spectrum, while reflection migration (smearing residuals along ellipse) fills in the high wavenumbers. Now we show that interbed multiples can fill in some of the intermediate wavenumbers denoted by the blue dots.

Fig. 12a depicts the interbed multiple rays for a thin-bed model with a diffractor at the lower interface. Each order of the multiple will be associated with a different mirror ray, where the depth of the mirror scatterer deepens with the order of the multiple. Therefore, the raypath lengthens with order of multiple, and the wavepath thickens as well. We conclude that the mirror wavepath that intersects the thin bed[7] thickens progressively with the order of the multiple, and so should fill in some of the "intermediate wavenumber" gap (Jannane et al., 1989) illustrated by the blue dots in Fig. 9.

The above analysis can be quantified as in the previous sections by analyzing the model resolution function. In this case, the forward modeling kernel $G(\mathbf{g}|\mathbf{x})G(\mathbf{x}|\mathbf{s})$ is replaced by one that generates an internal multiple rather than a direct wave or primary reflection.[8] The phase term in the Green's function will be replaced by a summation of times corresponding to each leg of the raypaths seen in Fig. 12a. The migration kernel is also modified by terms that will image the internal multiple to one of its bounce points in the thin layer.

5. Discussion and summary

Formulas are derived for the resolution limits of the migration-data kernels in Fig. 4, as well as those for multiple reflections. They are applicable to images formed by RTM, LSM, and FWI. Their salient implications are the following.

1. Low- and intermediate-wavenumber information about the velocity distribution is estimated primarily by transmission migration of primaries and multiples. The intermediate wavenumbers can be supplied by interbed multiples, while the lower wavenumbers are contained in deep primaries and free-surface related multiples. Inverting multiples can be an opportunity for estimating subsurface velocity information not available in the primary reflections.
2. Inverting diffractions can provide twice or more the resolution compared to imaging primaries. Smearing residuals along the transmission wavepath can achieve a resolution of λ near the diffractor. On the other hand, diffraction energy can be more than an order-of-magnitude weaker than primary energy, so the diffraction data will be noisier.
3. Diving waves that bottom out at a certain depth will have a better vertical resolution than horizontal resolution. Therefore, it is also important to invert deep reflections to increase both the vertical and horizontal resolution. Since reflections can be an order-of-magnitude weaker than diving waves, it is recommended that diving waves be filtered from the data after a sufficient number of iterations. This might constitute an iterative multi-physics approach to FWI, where inverting a different type of wavefield should be emphasized at different depths and iteration numbers.
4. The transmission migration kernels in Fig. 4a–d are of the same type as their data kernels. This leads to velocity updates along the transmission wavepaths. In contrast, the traditional migration kernel $[G(\mathbf{g}|\mathbf{x})^{dir}G(\mathbf{x}|\mathbf{s})^{dir}]^*$ in Fig. 4e is a product of two Green's functions for direct waves, while the data kernel is a product of a reflection and a direct-wave Green's function. This mismatch in the type of kernel does not lead to the traditional wavepath where seismic energy propagates, but gives the migration ellipse, which is the zone where reflection energy could have originated, i.e., the interface.

The limitation of this study is that it does not take into account the non-linear effects of evanescent energy (Fleming, 2008) in determining resolution. Utilizing evanescent energy with FWI could provide, in theory, resolution much better than λ. It is expected that multiple scattering arrivals between neighboring sub-wavelength scatterers might provide the extra resolution needed, but not accounted for in this current study.

Acknowledgment

Research reported in this publication was supported by King Abdullah University of Science and Technology (KAUST).

[7] The sampling interval between wavenumbers associated with each order of multiple becomes smaller with thinner beds.

[8] This kernel corresponds to just one of the terms in the Neumann series expansion of the Lippmann–Schwinger equation (Stolt and Benson, 1986).

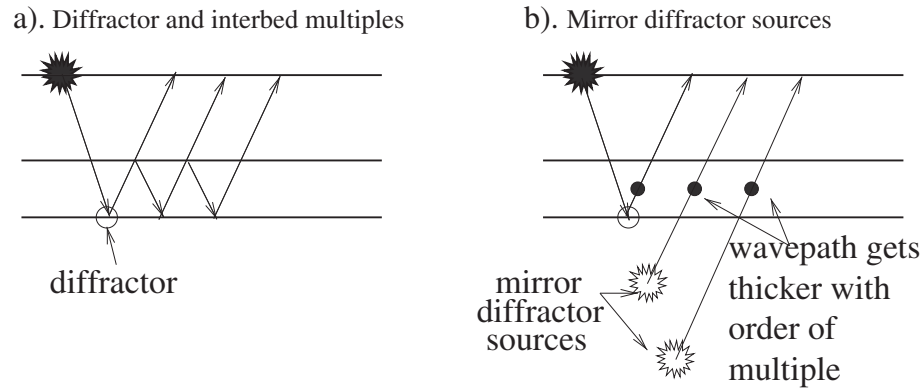

Fig. 12. a) Ray diagram for interbed multiples generated by a diffractor in a thin layer and b) the associated mirror sources diagram. As the order of the interbed multiple increases, so does the thickness of its transmission wavepaths at the filled circles •.

Appendix A. Resolution properties of Fresnel volume in constant and layered media

We first analyze the resolution of the ellipse depicted in Fig. 1b, and then relate the parameters of this ellipse to an ellipsoid and to those defining a wavepath. Lastly, we examine the case of multilayered media.

The spatial resolution limit near the point c in Fig. 1b is related to the reciprocal of the segment length $\overline{DE}$. This length can be determined by noting that the end points D and E satisfy both the equations of the ellipse and the line, written as

$$\frac{x^2}{a^2}+\frac{y^2}{b^2}=1, \tag{A.1}$$

$$y=\tan\theta(x-c), \tag{A.2}$$

where a and b are the major and minor radii of the ellipse, respectively, and θ is the angle DE makes with the axis of the ellipse. Eqs. (A.1) and (A.2) can be reduced to a quadratic equation of one variable y, yielding two roots y_D and y_E. The distance $\overline{DE}$ is then obtained as

$$\overline{DE}=\frac{|y_D-y_E|}{|\sin\theta|}, \\ =\frac{2ab\sqrt{b^2\cos^2\theta+\left(a^2-c^2\right)\sin^2\theta}}{b^2\cos^2\theta+a^2\sin^2\theta.} \tag{A.3}$$

Two special cases of c and θ are immediately verified. We have $\overline{DE}=2a$ when $\theta=0$, and $\overline{DE}=2b$ when $c=0$ and $\theta=\pi/2$, i.e., the lengths of the major and the minor axes of the ellipse, respectively.

In a homogeneous and isotropic medium, the Fresnel volume is a prolate spheroid, which is an ellipsoid that is rotationally symmetric around the major axis sg depicted in Fig. 1b. Therefore, Eq. (A.3) remains invariant with respect to this rotation. For an arbitrary line of intersection passing through the major axis, the steps to calculate the resolution are: (1) to find the intercept c and the angle θ as depicted in Figs. 1b, and (2) to use eq. (A.3) for the resolution calculation.

Next, the parameters a and b of the ellipse are related to those defining the first Fresnel zone, as depicted in Fig. 1a. Let s and g be the two foci of the ellipse, the distance between s and g be L, and E be an arbitrary point on the ellipse. The first Fresnel zone is delimited by points E on the ellipse that satisfy

$$\overline{sE}+\overline{Eg}=L+\frac{\lambda}{2}. \tag{A.4}$$

$$\text{Also,}\quad \overline{sE}+\overline{Eg}=2a \tag{A.5}$$

is a property of the ellipse. Another property of the ellipse relates the focal distance to the major and minor radii by

$$L=2\sqrt{a^2-b^2}. \tag{A.6}$$

Eqs. (A.4)–(A.6) give us

$$a=\frac{L}{2}+\frac{\lambda}{4}, \tag{A.7}$$

$$\text{and}\quad b=\sqrt{\frac{\lambda L}{4}+\frac{\lambda^2}{16}}. \tag{A.8}$$

In the limit of $L\gg\lambda$, $b\to\frac{1}{2}\sqrt{\lambda L}$.

From Eqs. (A.7), (A.8), and (A.3), we see that the resolution can be written as $\overline{DE}(L,\lambda,c,\theta)$, a function of wavepath parameters L, λ, and intersection parameters c and θ.

Lastly, in the case of multilayered media, as denoted by the brown lines in Fig. 1a, we rewrite Eq. (A.4) in terms of traveltimes (cf. Eq. (1)) as

$$\tau_{sE}+\tau_{Eg}=\tau_{sg}+T/2. \tag{A.9}$$

Here, the traveltimes can be computed approximately using the RMS velocity for N layers defined by

$$v_{\text{RMS}}=\sqrt{\frac{\sum_i^N v_i^2\Delta\tau_i}{\sum_i^N\Delta\tau_i}}, \tag{A.10}$$

where $\Delta\tau_i$ is the vertical 1-way time through the i^{th} layer. Note that in Fig. 1a, the v_{RMS} sensed from the source s to the reflector F is equal to that sensed from F to the receiver g. Write the 1-way vertical traveltime to the reflector F at depth d as $\tau(0)=\sum_i^N\Delta\tau_i$, and the traveltime equation for multilayered media is given as

$$\tau(x)\cong\sqrt{\tau(0)^2+x^2/v_{\text{RMS}}^2} \tag{A.11}$$

where x is a 1-way offset, e.g., $\overline{PE}$ in Fig. 1a. By introducing an effective depth

$$d_{\text{eff}}=\tau(0)v_{\text{RMS}}, \tag{A.12}$$

we can rewrite Eq. (A.11) as

$$\tau(x)\cong\frac{\sqrt{d_{\text{eff}}^2+x^2}}{v_{\text{RMS}}}. \tag{A.13}$$

This expression, which applies to every τ term in Eq. (A.9), coincides with the case of constant velocity v_{RMS} and reflector depth d_{eff}. Therefore, for the horizontal resolution at the reflector, the previous resolution analysis based on a constant medium can apply to multilayered media, with the transformations that

$$\lambda\rightarrow\lambda_{\text{RMS}}=v_{\text{RMS}}/f_0, \tag{A.14}$$

$$d\rightarrow d_{\text{eff}}=v_{\text{RMS}}\sum_i^N\Delta\tau_i, \tag{A.15}$$

where f_0 is the dominant frequency of the source wavelet. Undergoing such transformations, the effective geometry in Fig. 1a will change. Specifically,

$$L_{\text{eff}}\overset{\text{def}}{=}\overline{sg}_{\text{eff}}=\sqrt{X^2+4d_{\text{eff}}^2}, \tag{A.16}$$

$$\theta_{\text{eff}}=\arctan(2d_{\text{eff}}/X), \tag{A.17}$$

while c remains as 0 for this reflection geometry. The corresponding a_{eff} and b_{eff} can be computed from Eqs. (A.7) and (A.8). Finally, Eq. (A.3) can be used to compute the horizontal resolution as desired.

Appendix B. Resolution limits for imaging diving wave residuals

The resolution limits for imaging diving wave residuals are rigorously derived by multiplying the migration kernel in Fig. 4a by the expression for the diving wave arrival

$$\delta d(\mathbf{g}|\mathbf{s})=\omega^4\int_\Omega G(\mathbf{g}|\mathbf{y})^{dir}G(\mathbf{y}|\mathbf{s})^{dir}\delta m(\mathbf{y})dy^2, \tag{B.1}$$

where the integral over the model-space region Ω is approximated by the one over the region Ω_{gs}. Here, Ω_{gs} coincides with the yellow first Fresnel zone of the diving wave in Fig. 4a for the source–geophone pair denoted by $\mathbf{s}$ and $\mathbf{g}$. This approximation recognizes that only model perturbations within the first Fresnel zone of the diving wave will strongly affect the timing and/or amplitude of the diving wave arrival at $\mathbf{g}$.

Plugging Eq. (B.1) into Eq. (6) gives

$$\delta m(\mathbf{x})^{mig}=\omega^4\int_{D_{r_o}}\int_{\Omega_{gs}}\left[G(\mathbf{g}|\mathbf{x})^{dir}G(\mathbf{x}|\mathbf{s})^{dir}\right]^*G(\mathbf{g}|\mathbf{y})^{dir}G(\mathbf{y}|\mathbf{s})^{dir}\delta m(\mathbf{y})dy^2dx_gdx_s. \tag{B.2}$$

We now assume a localized sub-wavelength perturbation $\delta m(\mathbf{y})$ centered at $\mathbf{r}_o=(x_o,z_o)$ that is non-zero only within a fraction of a wavelength from $\mathbf{r}_o$. In this case, the range of source–geophone pairs in D is restricted to the set D_{r_o} of source–geophone pairs that allow for first Fresnel diving wavepaths to visit the localized perturbation centered at $\mathbf{r}_o$. These source–geophone pairs are the only ones whose transmitted diving waves[9] will be significantly influenced by the model perturbations centered at $\mathbf{r}_o$. For example, if the image point is at $\mathbf{y}$ and the geophone is at C in Fig. 6b, then D_{r_o} is limited to the sources between A and B.

For a smooth background velocity, we assume the following asymptotic Green's function for the migration and data kernels

$$G(\mathbf{x}|\mathbf{y})^{dir}=A_{xy}e^{-i\omega\tau_{xy}}, \tag{B.3}$$

so that Eq. (B.2) becomes

$$\delta m(\mathbf{x})^{mig}=\omega^4\int_{D_{r_o}}\int_{\Omega_{gs}}A_{sx}A_{gx}A_{sy}A_{gy}e^{i\omega\left(\tau_{gx}+\tau_{sx}-\tau_{gy}-\tau_{sy}\right)}\delta m(\mathbf{y})dy^2dx_gdx_s. \tag{B.4}$$

Here, τ_{xy} is the traveltime for the transmitted wave to propagate from $\mathbf{y}$ to $\mathbf{x}$, and A_{xy} is its attendant geometrical spreading term that satisfies the transport equation.

Assuming that the sub-wavelength scatterer represented by $\delta m(\mathbf{y})$ is located within a fraction of a wavelength from the trial image point at $\mathbf{x}$, then τ_{sy}, τ_{gy}, τ_{sx}, and τ_{gx}, can be expanded about its center point $\mathbf{r}_o$ to give

$$\begin{aligned}
\tau_{sy}&\approx\tau_{sr_o}+\nabla\tau_{sr_o}\cdot[\mathbf{y}-\mathbf{r}_o],\\
\tau_{gy}&\approx\tau_{gr_o}+\nabla\tau_{gr_o}\cdot[\mathbf{y}-\mathbf{r}_o],\\
\tau_{sx}&\approx\tau_{sr_o}+\nabla\tau_{sr_o}\cdot[\mathbf{x}-\mathbf{r}_o],\\
\tau_{gx}&\approx\tau_{gr_o}+\nabla\tau_{gr_o}\cdot[\mathbf{x}-\mathbf{r}_o].
\end{aligned} \tag{B.5}$$

Inserting these approximations into Eq. (B.4) gives

$$\delta m(\mathbf{x})^{mig}\approx\omega^4\int_{D_{r_o}}\int_{\Omega_{gs}}A_{sx}A_{gx}A_{sy}A_{gy}e^{-i\omega\left(\nabla\tau_{gr_o}+\nabla\tau_{sr_o}\right)\cdot[\mathbf{y}-\mathbf{x}]}\delta m(\mathbf{y})dy^2dx_gdx_s.$$

Under the far-field approximation, the geometric spreading terms can be taken outside the integral to give

$$\begin{aligned}
\delta m(\mathbf{x})^{mig}&=\omega^4\int_{D_{r_o}}A_{sx}A_{gx}A_{sr_o}A_{gr_o}\int_{\Omega_{gs}}e^{-i\omega\left(\nabla\tau_{gr_o}+\nabla\tau_{sr_o}\right)\cdot[\mathbf{y}-\mathbf{x}]}\delta m(\mathbf{y})dy^2dx_gdx_s.\\
&\approx\omega^4\int_{\Omega_{gs}}G(\mathbf{g}|\mathbf{y})^{dir}G(\mathbf{y}|\mathbf{s})^{dir}\delta m(\mathbf{y})dy^2,
\end{aligned} \tag{B.6}$$

Here, the gradient of the traveltime field $\nabla\tau_{sr_o}$ is parallel to the direct wave's incident angle at $\mathbf{r}_o$, so, according to the dispersion equation, $\omega\nabla\tau_{sr_o}=\mathbf{k}_{sr_o}$ can be identified as the source-to-scatterer point wavenumber vector $\mathbf{k}_{sr_o}$; similarly, the geophone-to-scatterer wavenumber is denoted as $\omega\nabla\tau_{gr_o}=\mathbf{k}_{gr_o}$. This means that, by definition of the Fourier transform with a restricted domain of integration $\delta M(\mathbf{k})=\int_{\Omega_{gs}}e^{-i\mathbf{k}\cdot\mathbf{y}}\delta m(\mathbf{y})dy^2$, Eq. (B.6) becomes

$$\delta m(\mathbf{x})^{mig}\approx\omega^4A_{s_og_or_o}^4\int_{D_{r_o}}e^{i\left(\mathbf{k}_{gr_o}+\mathbf{k}_{sr_o}\right)\cdot\mathbf{x}}\delta M\left(\mathbf{k}_{gr_o}+\mathbf{k}_{sr_o}\right)dx_gdx_s, \tag{B.7}$$

where $A_{s_og_or_o}$ approximates the geometrical spreading for the scatterer at $\mathbf{r}_o$ with the range of allowable source–geophone pairs centered around the pairs denoted by s_og_o, the Fourier spectrum of the model is given by $\delta M(\mathbf{k})$, and the model wavenumber components $\mathbf{k}=(k_x,k_z)$ are

$$\begin{aligned}
k_x&=k_{sx_o}+k_{gx_o}=\omega s(\mathbf{r}_o)\left(\sin\beta_{sr_o}+\sin\beta_{gr_o}\right),\\
k_z&=k_{sz_o}+k_{gz_o}=\omega s(\mathbf{r}_o)\left(\cos\beta_{sr_o}+\cos\beta_{gr_o}\right),
\end{aligned} \tag{B.8}$$

where β_{sr_o} and β_{gr_o} denote the incidence angles of the source and geophone rays, respectively, at the scatterer's location $\mathbf{y}=(x_o,z_o)$. As shown in this appendix, these incidence angles are implicit functions of the source $(x_s,0)$, geophone $(x_g,0)$, and scatterer $\mathbf{r}_o=(x_o,z_o)$ coordinates.

[9] We exclude the case where the scatterer–diving wave interaction produces significant diffractions, so that all source–geophone pairs see significant diffraction energy, not just changes in the diving wave arrival. This would be the case where the scatterer only has a velocity contrast but no impedance contrast.

The determinant of the Jacobian in Eq. (C.2) (see Appendix C) can be used to map the $dx_g dx_s$ integration in Eq. (B.7) to a $dk_x dk_z$ integration:

$$\delta m(\mathbf{x})^{mig} = \omega^4 A^4_{s_o g_o r_o} \int_{\mathcal{D}_{r_o}} e^{-i\mathbf{k}\cdot\mathbf{x}}\, \delta M(\mathbf{k}) J^{-1} dk_x dk_z, \tag{B.9}$$

where $\mathcal{D}_{r_o}$ is the set of wavenumbers that Eq. (B.8) maps from the source–geophone pairs in D_{r_o} for the scatterer at $\mathbf{r}_o$, and J is the determinant of the Jacobian matrix in Eq. (C.2).

Appendix C. Determinant of a Jacobian matrix

The transformation between the data coordinates $(x_g, 0)$, $(x_s, 0)$ and $(k_x, k_z) = (k_{sx_o} + k_{gx_o}, k_{sz_o} + k_{gz_o})$ is given by

$$\begin{pmatrix} dk_x \\ dk_z \end{pmatrix} = \begin{bmatrix} \frac{\partial k_x}{dx_g} & \frac{\partial k_x}{dx_s} \\ \frac{\partial k_z}{\partial x_g} & \frac{\partial k_z}{\partial x_s} \end{bmatrix} \begin{pmatrix} dx_g \\ dx_s \end{pmatrix}, \tag{C.1}$$

where the 2×2 matrix is the Jacobian matrix. The scaled determinant J of the Jacobian matrix is given by

$$J = \omega^4 \left| \frac{\partial k_x}{dx_g} \frac{\partial k_z}{\partial x_s} - \frac{\partial k_x}{dx_s} \frac{\partial k_z}{\partial x_g} \right|, \tag{C.2}$$

so that $dk_x dk_z = J dx_g dx_s$. In the case of a homogeneous medium with velocity c and a scatterer at $\mathbf{r}_o = (x_o, z_o)$, the model wavenumbers are

$$\begin{aligned} k_x &= \frac{\omega\left(x_o - x_g\right)}{c\sqrt{\left(x_o - x_g\right)^2 + z_o^2}} + \frac{\omega(x_o - x_s)}{c\sqrt{(x_o - x_s)^2 + z_o^2}}, \\ k_z &= \frac{\omega z_o}{c\sqrt{\left(x_o - x_g\right)^2 + z_o^2}} + \frac{\omega z_o}{c\sqrt{(x_o - x_s)^2 + z_o^2}}, \end{aligned} \tag{C.3}$$

so that the partial derivatives of the wavenumbers can be easily determined. For a heterogeneous medium, the derivatives can be approximated by finite-difference approximations to the first-order derivatives and the wavenumbers can be computed by a ray tracing method. Under the far-field approximation $z \gg L$, where L is the aperture width of the source–geophone array, so Eq. (C.3) becomes

$$\begin{aligned} k_x &\approx \frac{\omega\left(x_o - x_g\right)}{c z_o} + \frac{\omega(x_o - x_s)}{c z_o}, \\ k_z &\approx \frac{2\omega}{c}, \end{aligned} \tag{C.4}$$

where the horizontal wavenumbers are now linear functions of the data variables x_g and x_s. This means that Eq. (B.7) represents the inverse Fourier transform of the model spectrum.

References

Baysal, E., Kosloff, D.D., Sherwood, J.W.C., 1983. Reverse time migration. Geophysics 48, 1514–1524.

Berkhout, A.J., 1984. Seismic Resolution: A Quantitative Analysis of Resolving Power of Acoustical Echo Techniques. Geophysical Press.

Beylkin, G., 1985. Imaging of discontinuities in the inverse scattering problem by inversion of a causal generalized radon transform. J. Math. Phys. 26, 99–108.

Buddensiek, M.L., Sheng, J., Crosby, T., Schuster, G., Bruhn, R., He, R., 2008. Colluvial wedge imaging using traveltime and waveform tomography along the Wasatch Fault near Mapleton, Utah. Geophys. J. Int. 172, 686–697.

Bunks, C., Saleck, F.M., Zaleski, S., Chavent, G., 1995. Multiscale seismic waveform inversion. Geophysics 60, 1457–1473.

Cerveny, V., Soares, J.E.P., 1992. Fresnel volume ray tracing. Geophysics 57, 902–915.

Chen, J., Schuster, G.T., 1999. Resolution limits of migrated images. Geophysics 64, 1046–1053.

Claerbout, J., 1992. Earth Soundings Analysis: Processing Versus Inversion. Blackwell Scientific Publications, Cambridge, Massachusetts.

Dahlen, F., 2004. Resolution limit of traveltime tomography. Geophys. J. Int. 157, 315–331.

Dai, W., Schuster, G.T., 2013. Reverse time migration of prism waves for salt flank delineation. SEG Technical Program Expanded Abstracts, pp. 3861–3865.

Dai, W., Fowler, P., Schuster, G.T., 2012. Multi-source least-squares reverse time migration. Geophys. Prospect. 60, 681–695.

de Fornel, F., 2001. Evanescent Waves: From Newtonian Optics to Atomic Optics. Springer.

De Hoop, M., van Der Hilst, R.D., 2005. On sensitivity kernels for wave-equation transmission tomography. Geophys. J. Int. 160, 621–633.

Devaney, A., 1984. Geophysical diffraction tomography. IEEE Trans. Geosci. Remote Sens. GE-22, 3–13.

Duquet, B., Marfurt, K.J., Dellinger, J., 2000. Kirchhoff modeling, inversion for reflectivity, and subsurface illumination. Geophysics 65, 1195–1209.

Fichtner, A., 2011. Full Seismic Waveform Modelling and Inversion. Springer.

Fichtner, A., Trampert, J., 2011a. Hessian kernels of seismic data functionals based upon adjoint techniques. Geophys. J. Int. 185, 775–798.

Fichtner, A., Trampert, J., 2011b. Resolution analysis in full waveform inversion. Geophys. J. Int. 187, 1604–1624.

Fichtner, A., Kennett, B.L., Igel, H., Bunge, H.P., 2009. Full seismic waveform tomography for upper-mantle structure in the Australasian region using adjoint methods. Geophys. J. Int. 179, 1703–1725.

Fink, M., 2008. Time-reversal waves and super resolution. Journal of Physics: Conference Series. IOP Publishing, p. 012004. http://dx.doi.org/10.1088/1742-6596/124/1/012004.

Fleming, M., 2008. Far-field super resolution. Ph.D. thesis. Imperial College London.

Harlan, W.S., 1990. Tomographic estimation of shear velocities from shallow cross-well seismic data. SEG Technical Program Expanded Abstracts, pp. 86–89.

Jannane, M., Beydoun, W., Crase, E., Cao, D., Koren, Z., Landa, E., Mendes, M., Pica, A., Noble, M., Roeth, G., et al., 1989. Wavelengths of earth structures that can be resolved from seismic reflection data. Geophysics 54, 906–910.

Kravtsov, Y.A., Orlov, Y.I., 1990. Geometrical Optics of Inhomogeneous Media. Springer-Verlag.

Krebs, J.R., Anderson, J.E., Hinkley, D., Neelamani, R., Lee, S., Baumstein, A., Lacasse, M.D., 2009. Fast full-wavefield seismic inversion using encoded sources. Geophysics 74, WCC177–WCC188. http://dx.doi.org/10.1190/1.3230502.

Lailly, P., 1984. Migration methods: partial but efficient solutions to the seismic inverse problem. Inverse problems of acoustic and elastic waves 51, pp. 1387–1403.

Liu, F., Zhang, G., Morton, S.A., Leveille, J.P., 2011. An effective imaging condition for reverse-time migration using wavefield decomposition. Geophysics 76, S29–S39.

Luo, Y., 1991. Calculation of wavepaths for band-limited seismic waves. SEG Technical Program Expanded Abstracts, pp. 1509–1512.

Luo, Y., Schuster, G.T., 1991. Wave-equation traveltime inversion. Geophysics 56, 645–653.

Marquering, H., Dahlen, F., Nolet, G., 1999. Three-dimensional sensitivity kernels for finite-frequency traveltimes: the banana-doughnut paradox. Geophys. J. Int. 137, 805–815.

McMechan, G., 1983. Migration by extrapolation of time-dependent boundary values. Geophys. Prospect. 31, 413–420.

Menke, W., 1989. Geophysical Data Analysis: Discrete Inverse Theory. Elsevier.

Mora, P., 1988. Elastic wave-field inversion of reflection and transmission data. Geophysics 53, 750–759.

Mora, P., 1989. Inversion = migration + tomography. Geophysics 54, 1575–1586.

Nemeth, T., Wu, C., Schuster, G., 1999. Least-squares migration of incomplete reflection data. Geophysics 64, 208–221.

Pica, A., Diet, J., Tarantola, A., 1990. Nonlinear inversion of seismic reflection data in a laterally invariant medium. Geophysics 55, 284–292.

Pratt, R.G., Goulty, N.R., 1991. Combining wave-equation imaging with traveltime tomography to form high-resolution images from crosshole data. Geophysics 56, 208–224.

Safar, M.H., 1985. On the lateral resolution achieved by Kirchhoff migration. Geophysics 50, 1091–1099.

Schuster, G.T., 1996. Resolution limits for crosswell migration and traveltime tomography. Geophys. J. Int. 127, 427–440.

Schuster, G.T., Hu, J., 2000. Green's function for migration: continuous recording geometry. Geophysics 65, 167–175. http://dx.doi.org/10.1190/1.1444707.

Schuster, G.T., Hanafy, S., Huang, Y., 2012. Theory and feasibility tests for a seismic scanning tunneling macroscope. Geophys. J. Int. 190, 1593–1606.

Sheley, D., Schuster, G.T., 2003. Reduced-time migration of transmitted Ps waves. Geophysics 68, 1695–1707.

Sheng, J., Schuster, G.T., 2003. Finite-frequency resolution limits of wave path traveltime tomography for smoothly varying velocity models. Geophys. J. Int. 152, 669–676.

Shin, C., Cha, Y.H., 2008. Waveform inversion in the Laplace domain. Geophys. J. Int. 173, 922–931.

Sirgue, L., Pratt, R.G., 2004. Efficient waveform inversion and imaging. A strategy for selecting temporal frequencies. Geophysics 69, 231–248.

Stolt, R.H., Benson, A.K., 1986. Seismic Migration: Theory and Practice. Pergamon Press.

Y.Tang, Y., 2009. Target-oriented wave-equation least-squares migration/inversion with phase-encoded HessianGeophysics 74, WCA95–WCA107. http://dx.doi.org/10.1190/1.3204768.

Tape, C., Liu, Q., Maggi, A., Tromp, J., 2009. Adjoint tomography of the Southern California crust. Science 325, 988–992.

Tarantola, A., 1984. Inversion of seismic reflection data in the acoustic approximation. Geophysics 49, 1259–1266.

Tarantola, A., 2005. Inverse Problem Theory and methods for model parameter estimation. SIAM.
J.Tong, J., F.Dahlen, F., G.Nolet, G., H.Marquering, H., 1998. Diffraction effects upon finite-frequency travel times: a simple 2-D exampleGeophys. Res. Lett. 25, 1983–1986.
Van Der Hilst, R.D., Maarten, V., 2005. Banana-doughnut kernels and mantle tomography. Geophys. J. Int. 163, 956–961.
Vermeer, G.J.O., 1997. Factors affecting spatial resolution. SEG Technical Program Expanded Abstracts, pp. 27–30.
Virieux, J., Operto, S., 2009. An overview of full-waveform inversion in exploration geophysics. Geophysics 74, WCC1.
Whitmore, N., 1983. Iterative depth migration by backward time propagation. SEG Technical Program Expanded Abstracts, pp. 382–385.
Williamson, P.R., 1991. A guide to the limits of resolution imposed by scattering in ray tomography. Geophysics 56, 202–207.
Woodward, M., 1989. Wave equation tomography. Ph.D. thesis. Stanford University.
M.Woodward, M., 1992. Wave-equation tomographyGeophysics 57, 15–26.
Wu, R.S., Toksoz, M.N., 1987. Diffraction tomography and multisource holography applied to seismic imaging. Geophysics 52, 11–25.
Zhan, G., Dai, W., Zhou, M., Luo, Y., Schuster, G.T., 2014. Generalized diffraction-stack migration and filtering of coherent noise. Geophys. Prospect. http://dx.doi.org/10.1111/1365-2478.12086 (online).
Zhang, S., Schuster, G., Luo, Y., 2012. Angle-domain migration velocity analysis using wave equation reflection traveltime inversion. SEG Technical Program Expanded Abstracts, pp. 1–6.
Zhou, C., Cai, W., Luo, Y., Schuster, G.T., Hassanzadeh, S., 1995. Acoustic wave-equation traveltime and waveform inversion of crosshole seismic data. Geophysics 60, 765–773.